Journal of Sound and Vibration (1999) **221**(2), 289–307
Article No. jsvi.1998.2010, available online at http://www.idealibrary.com on IDEAL

DESTABILIZING EFFECTS OF RATE FEEDBACK ON STRAIN ACTUATED BEAMS

O. S. Alvarez-Salazar
Flight Systems Research Center, *UCLA*, *MC* 951594, *Los Angeles*, *CA* 90095, *U.S.A.*

AND

K. Iliff
Dryden Flight Research Center, *NASA*, *MS D*2033, *Edwards*, *CA* 93523, *U.S.A.*

(*Received* 12 *January* 1998, *and in final form* 13 *October* 1998)

The stabilizing and destabilizing effects of rate feedback control on all modes of a strain actuated beam are demonstrated here to support earlier theoretical findings by Balakrishnan [1] (1999 *Journal of Computational and Applied Mathematics* **18**). The destabilizing effects being due to the actual implementation of the rate feedback controller which is unavoidably non-ideal. The main contribution here is the inclusion of the controller circuit model in the closed loop system equations to obtain correct stability estimates for all modes. Closed loop stability estimates computed from this *circuitry enhanced model* were corroborated by experiments. The strain actuated beam constructed for this work was made with a fiber glass lay-up and piezo ceramic wafers embedded throughout the length of the lay-up. A charge-to-voltage amplifier, a differentiator, a gain stage, and a power amplifier were also constructed. The most crucial of these components was the differentiator and its tank frequency. The first four modes and transmission zero frequencies, and the corresponding structural damping were obtained through open loop experiments. Mode estimates were within 5% of the computed values. Zero estimates were less accurate due to electric feedthrough, but modelling of this effect helped to improve zero frequency estimates. Closed loop experiments were run to demonstrate the destabilization of beam modes with frequencies higher than the differentiator's tank frequency.

1. INTRODUCTION

The problem of stabilizing a clamped–free bending beam with a straining actuator and/or sensor has been previously considered and has now become the canonical problem in strain actuated structures. Bailey and Hubbard [2] were the first to consider the problem. In their work they bonded a layer of polyvinylidene fluoride, PVF_2, material onto a steel beam and with the use of an accelerometer at the free end of the beam were able to actively stabilize it. However, only the first few modes of the beam were considered in their experiments. Their controller design (using Lyapunov's second method) showed that rate feedback of the beam's tip curvature would maximize energy dissipation.

0022–460X/99/120289 + 19 $30.00/0

Tzou *et al*. [3, 4] bonded layers of PVF_2 onto both surfaces of a cantilevered plexiglas bending beam. The active material was bonded on the beam from its clamped end to its free end, and one of the layers was used as an actuator and the other as a sensor. Since the sensor signal output was shown to be proportional to the slope of the beam at its tip, the signal was differentiated, amplified and directly fed into the actuator layer. Tzou *et al*.'s modelling and analysis of the system correctly predicted the dependence of damping on the gain of the feedback loop, and their experiment validated their simulations (first mode only).

Lee *et al*. [5] considered the problem of PVF_2 sensor/actuator shaping for a cantilevered beam and showed how *critical* damping could be achieved for a chosen mode. In their paper they also showed that only 3·3% damping could be achieved for the first mode whenever the sensor/actuator pair was uniformly shaped over the entire length of the beam (i.e., no shaping). After shaping the sensor and actuator pair, Lee and company increased the attainable damping of the beam to 17·6% for the first mode. They also found it possible to increase the damping to 100% if a shielded sensor/actuator pair was used (electrical coupling, or feedthrough, limits system performance). As in reference [2], Lee used a stainless steel beam for the experiments, and he only considered the first mode.

The problem considered here is the stabilization and destabilization via rate feedback of a fiber glass bending beam with clamped–free boundary conditions. The beam has piezo ceramic wafers (PZT) embedded in its lay-up as opposed to PVF_2 bonded on its surface. The wafers were configured such that a sensor/actuator pair, uniformly shaped, runs the entire length of the beam (from clamped to free end).

Theoretical aspects underlying this problem were treated by Balakrishnan [1], who modelled the beam using the Euler formulation. Balakrishnan showed that results obtained by Tzou *et al*. [4] were correct. However, damping performance limitations due to the fact that exact differentiation of the sensor output is not possible (a band limited approximation is used instead) were also studied by Balakrishnan for the first time in the context of self-straining structures. In other words, modelling of the electronics used to implement the rate feedback controller coupled with the continuum model of the beam, sensor, and actuator were used to analyze stability for all system modes (not just the first two or three). Thus, Balakrishnan's modelling of controller electronics yielded a *circuitry enhanced model* for strain actuated structures. This technique, although cumbersome in more complicated systems, can be generalized to all structural control systems to predict high frequency controller effects (i.e., spillover).

Rate feedback implementation issues (i.e., a perfect differentiator cannot be built) were also shown by Balakrishnan to change the characteristics of the problem. In particular, it was shown that the approximate differentiator used does not yield a stable closed loop system. More precisely, all modes of the closed loop beam whose frequencies were higher than the tank frequency of the rate feedback circuit were shown to be unstable; on the other hand, all modes of the closed loop beam whose frequencies were lower than such tank frequency were shown to be stable.

Experimental and computational results corroborating Balakrishnan's analytical findings are presented here. Details related to the experimental hardware are first presented in sections 2–4. Then, the system's *circuitry enhanced model* and a summary of important analytical results are given in section 5. Experimental results are presented in sections 6 and 7, while conclusions and recommendations are given in section 8.

2. BEAM CONSTRUCTION

The beam used in this work was made with fiber glass cloth and PZT wafers. The fiber glass was style 112. Cloth thickness was 76·2 (10^{-6}) m (0·003 in.). The PZT wafers were Navy Type V from Vernitron Inc. Each wafer was 381 (10^{-6}) m (0·015 in.) thick, 63·5 (10^{-3}) m ($2\frac{1}{2}$ in.) long and 31·8 (10^{-3}) m (1 in.) wide.

The beam was fabricated in three stages. In the first stage, a fiber glass core was fabricated using the fiber glass cloth. The core was 795 (10^{-6}) m ($\frac{1}{32}$ in.) thick, 46 (10^{-3}) m (1·8 in.) wide and 0·694 m ($27\frac{5}{16}$ in.) long. In the second stage, four separate PZT implants were constructed by cutting eight "compartments" in a fiber glass lay-up (794 (10^{-6}) m thick).

The compartments were cut in such a way that only the center five fiber glass layers of cloth were removed. Thus, each compartment was just as deep as the thickness of a PZT wafer. The compartments were cut in a single row along the "x" axis of the beam; see Figure 1. The separation between compartments was

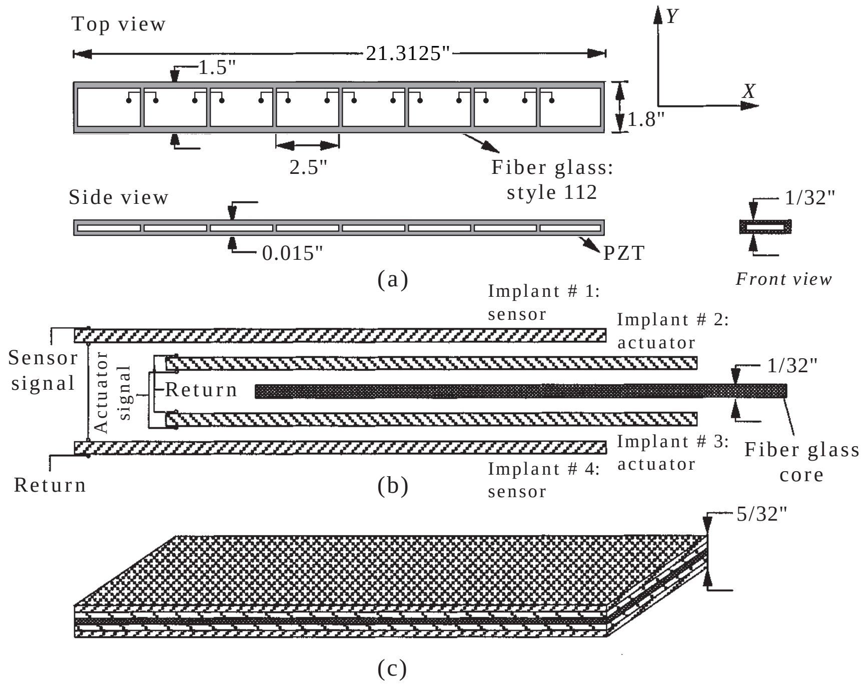

Figure 1. Beam construction: (a) PZT implant layup, (b) implant configuration, (c) implant assembled into beam.

3·2 (10^{-3}) m ($\frac{1}{8}$ in.), and the first one was cut at one end of the beam. The compartments were also made such that the long (straining) axis of the wafers was aligned with the "*x*" axis of the beam.

For each implant, one PZT wafer was placed in each of the compartments with the same direction of polarity as the other wafers. Since each wafer has a positive and negative face, all the positive faces were electrically connected via a silver ribbon and the negative faces were done in the same way.

Finally, in the third stage, the goal was to put together the core and the implants and cure the lay-up in an oven. The final lay-up consisted of two implants on each side of the core. Figure 1 shows a schematic of how the beam was made. Note that the resulting beam is approximately 396·9 (10^{-6}) m ($\frac{5}{32}$ in.) thick, 0·694 m ($27\frac{5}{16}$ in.) long and 45·7 (10^{-3}) m (1·80 in.) wide. Also, note that the PZT wafers only cover 0·541 m ($21\frac{5}{16}$ in.) of the beam (including compartment separations); this is the "active" portion of the beam. The remaining length was designed to clamp the beam, and it is not shown in Figure 1.

To clamp the beam a pair of 19·1 (10^{-3}) m ($\frac{3}{4}$ in.) thick aluminum square plates (0·15 m per side) were cut, and the "clamping" portion of the beam was placed between them using six bolts and nuts. The plates were then bolted to an optical table. The clamped beam measured 0·541 m ($21\frac{5}{16}$ in.) long from root to free end.

3. SENSOR AND ACTUATOR CONFIGURATION

Initially, the PZT sensor and PZT actuator on the beam were configured each from two implants. The two implants closest to the core (one per side of the beam) formed the actuator, and the remaining two implants formed the sensor. Electrically, the implants for the sensor were connected in "series" to maximize their voltage output, and the implants for the actuator were connected in "parallel" to maximize their stroke (see Figure 1). However, this configuration produced too much electrical feedthrough between the sensor and the actuator. Thus, to reduce the feedthrough effect, only two of the implants were used, one implant from each side of the beam. Although this reduced the feedthrough effect, it did not eliminate it. Figure 2 shows the beam with the correct sensor/actuator configuration.

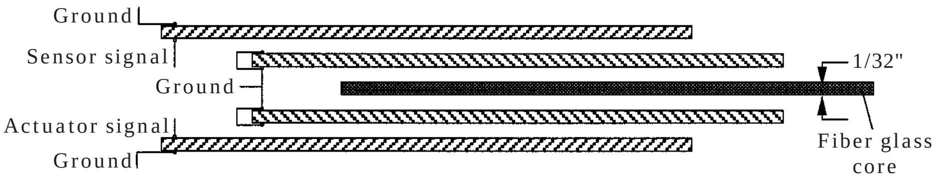

Figure 2. Sensor/actuator configuration.

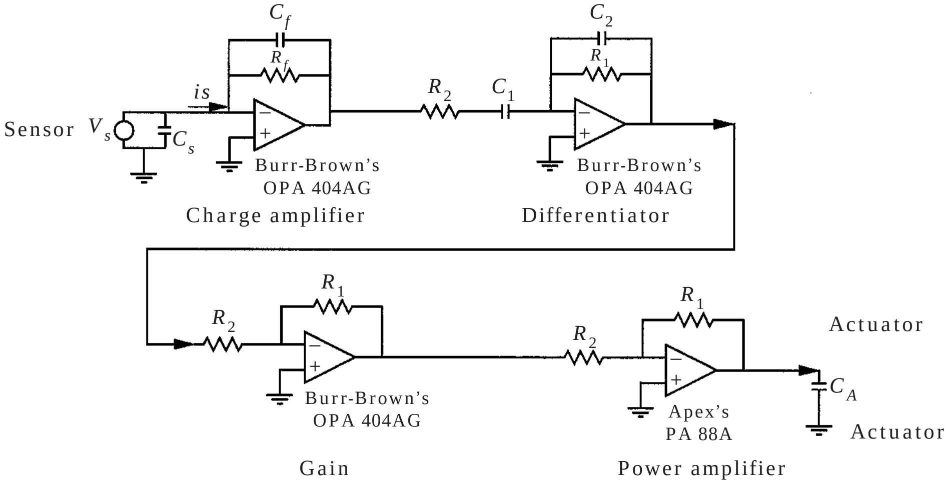

Figure 3. Control electronics.

4. ELECTRONICS

The electronics hardware built consisted of a charge-to-voltage amplifier, a differentiator, a variable gain stage, and a power amplifier. Figure 3 shows a schematic of the circuitry built.

Note that since an ideal differentiator cannot be implemented, the differentiator circuit shown in Figure 3 is only an approximation. A typical transfer function plot of this differentiator and the equivalent circuit used to model it in closed loop computations is shown in Figure 4. The most important feature of the differentiator used here is its tank frequency (an ideal differentiator does not have one). As mentioned earlier, the tank frequency is important because all mode frequencies of the beam lower than this frequency are stabilized, and all mode frequencies beyond this frequency are destabilized.

5. THEORY

In this section a *circuitry enhanced model*, open loop, and closed loop transfer functions for the smart beam and feedback electronics described in sections 2–4

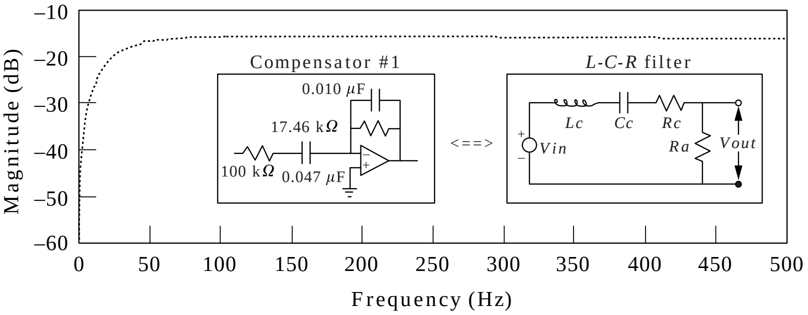

Figure 4. Transfer function Bode plot of differentiator.

are given. The electrical feedthrough from actuator to sensor is also modelled and its effect on system response is studied. Root locus analysis of the system is used to show the dependence of modal stability on the tank frequency of the feedback circuitry. Finally, sample root loci computations are given to corroborate theoretical and experimental results.

5.1. CIRCUITRY ENHANCED MODEL

Following the work of Balakrishnan [1], and earlier developments in the field of smart structures [2–8] the Euler–Bernoulli beam model is used here with boundary conditions corresponding to a clamped–free beam. The control law is rate feedback, with the control effort being proportional to the time derivative of the charge across the PZT sensor. Letting $f(t, x)$, $0 < x < l$ (where l is the beam's length), denote the deflection of the beam normal to the x-axis (see Figure 5), the closed loop model takes on the form

$$m\ddot{f}(t, x) + EIf''''(t, x) = 0, \qquad 0 < x < l,$$

$$f(t, 0) = f'(t, 0) = f'''(t, l) = 0, \qquad EIf''(t, l) + \alpha\dot{q}(t) + v_e(t) = 0, \tag{1}$$

where m, E and I are the mass per unit length, the Young's modulus, and the moment of inertia for the beam respectively. α is the closed loop gain, $q(t)$ is the charge in the sensor, and $v_e(t)$ is the system excitation. Both $\alpha\dot{q}(t)$ and $v_e(t)$ constitute the PZT actuator total moment applied to the beam at its free end.

The charge in the sensor, $q(t)$, is related to $f(t, x)$ through the following feedback circuit equation:

$$\frac{q(t)}{C} + R\dot{q}(t) + L\ddot{q}(t) = v(t),$$

$$v(t) = v_s(t) + \varepsilon\chi_A f''(t, l), \qquad v_s(t) = \chi_s \int_0^l W(s) f''(t, s)\,\mathrm{d}s, \tag{2}$$

where C, R and L are the equivalent capacitance, resistance and inductance of the rate feedback circuit respectively. $v(t)$ is the PZT sensor voltage output taken at

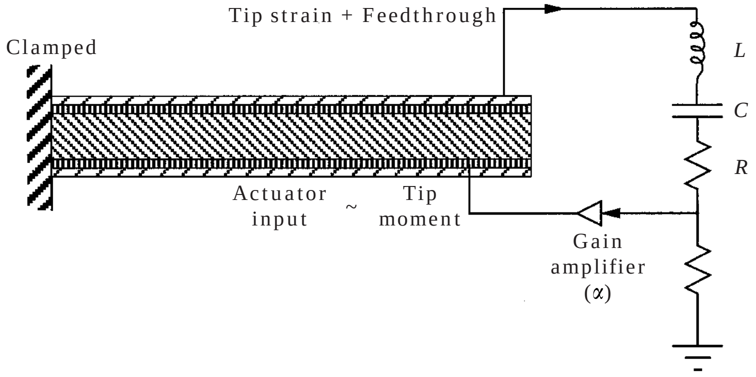

Figure 5. Block diagram of closed loop system: ▨, sensor; ▥, actuator; ▧, beam's core.

the output of the charge amplifier (see Figure 3). $W(s)$ is the sensor shape function which is equal to one for the beam constructed here [1, 5]. χ_s and χ_A are constants relating the voltage across the sensor and the actuator input voltage to the function $f(t, x)$. Equation (2) also includes the electrical feedthrough from actuator to sensor which is proportional, $\varepsilon > 0$ being the proportionality constant, to the tip moment applied by the actuator to the beam. Equations (1) and (2) constitute the *circuitry enhanced model* for the system.

Evident by inspection of equation (2) is the existence of a tank frequency associated with the strain rate feedback electronics. The tank frequency can be computed as

$$w_c = \sqrt{\frac{1}{LC}}\,. \tag{3}$$

An open loop system input–output model, the input being the tip moment applied by the PZT actuator and the output being $v(t)$, yields the following transfer function (with $W(s)$ in equation (2) set to one):

$$\psi_{Open}(\lambda) = \frac{V_s(\lambda) + \varepsilon V_e(\lambda)}{V_e(\lambda)} = \frac{\chi_s f''(\lambda, l) + \varepsilon\chi_A f''(\lambda, l)}{\chi_A f''(\lambda, l)}\,, \tag{4}$$

and the solution of equation (1), with α set to zero, yields

$$\psi_{Open}(\lambda) = \frac{\chi_s[\sinh(\gamma\cdot l)\cos(\gamma\cdot l) + \cosh(\gamma\cdot l)\sin(\gamma\cdot l)] + \chi_F\gamma[1 + \cosh(\gamma\cdot l)\cos(\gamma\cdot l)]}{\chi_A\gamma[1 + \cosh(\gamma\cdot l)\cos(\gamma\cdot l)]}\,, \tag{5}$$

where

$$\gamma = \sqrt{|\gamma| v}\ \mathrm{e}^{i\theta/2}\,\mathrm{e}^{i\pi/4}, \qquad \lambda = |\lambda|\,\mathrm{e}^{i\theta},$$

$$v^2 = \frac{m}{EI}\,, \qquad \chi_F = \varepsilon\chi_A\,. \tag{6}$$

The “poles” of the open loop system are given by zeros of the denominator of equation (5), and are denoted $\{\pm i w_k\}$.

The “zeros” of the system are given by the zeros of the numerator of equation (5) and are denoted $\{\pm i\tilde{\tilde{w}}_k\}$.

Clearly, the electrical feedthrough can only affect the zeros of the open loop system (i.e., the poles of the transfer function are unchanged).

A closed loop system input–output model yields the transfer function

$$\psi_{Closed}(\lambda) = \frac{EI\psi_{Open}(\lambda)}{EI + \alpha C\lambda(\psi_{Open}(\lambda)/p(\lambda))}\,, \tag{7}$$

where

$$p(\lambda) = (1 + CR\lambda + CL\lambda^2). \tag{8}$$

As in the open loop case, the poles of the closed loop system are computed from the denominator of equation (7) and are denoted

$$\{\lambda_k\} = \{\sigma_k(\alpha) + i w_k(\alpha)\}. \tag{9}$$

TABLE 1

System properties

$EI = 10{\cdot}46$ N-m^2 ($3647{\cdot}89$ Lbf-in.^{2})
$m = 0{\cdot}649$ kg/m ($1{\cdot}13 \times 10^{-3}$ slugs/in.)
$\varepsilon = 0{\cdot}0022$
$L = 0{\cdot}541$ m ($21{\cdot}3125$ in.)
$\chi_s = 419{\cdot}584$
$\chi_A = 775\,157{\cdot}246$
$\chi_F = \varepsilon\chi_A$
$C = 0{\cdot}82 \times 10^{-3}$
$RC = 4{\cdot}054 \times 10^{-3}$
$LC = 0{\cdot}82 \times 10^{-6}$

The zeros of equation (7) remain unchanged.

For future reference, beam parameters are summarized in Table 1. The differentiator parameters used in simulations are also summarized in this table.

5.2. EFFECT OF ε ON THE OPEN LOOP TRANSFER FUNCTION

In this section the electrical feedthrough from actuator to sensor, ε, is shown to reduce the frequencies of the zeros of the transfer function.

A partial fraction expansion for the system's open loop transfer function, equation (4) with $\varepsilon = 0$, is given by

$$\tilde{\psi}(\lambda) = \psi_{Open}(\lambda)|_{\varepsilon=0} = \frac{\chi_s f'(\lambda, l)}{\chi_A f''(\lambda, l)} = \sum_1^{\infty} \frac{b_k \omega_k^2}{\lambda^2 + \omega_k^2}, \tag{10}$$

where

$$b_k = \frac{4}{l} \frac{(\cosh(\gamma_k \cdot l) - 1)}{(\cosh(\gamma_k \cdot l) + 1)} \frac{1}{\omega_k v} > 0, \qquad \text{for every } k. \tag{11}$$

From equations (10) and (11) it follows that $\lambda\tilde{\psi}(\lambda)$ is positive real (i.e., $\mathrm{Re}\,[\lambda\tilde{\psi}(\lambda)] > 0$ for $\mathrm{Re}\,\lambda > 0$). (This can be readily seen by inspection of $\mathrm{Re}\,[\lambda/(\lambda^2 + \omega_k^2)]$ which is positive or zero for every k.) Moreover, since

$$-\lambda\tilde{\psi}(-\lambda) = -\lambda\tilde{\psi}(\lambda),$$

the zeros of $\lambda\tilde{\psi}(\lambda)$ must be on the imaginary axis. Now, let $\{\pm i\tilde{\omega}_k\}$ denote the zeros of $\tilde{\psi}(\lambda)$. Then, from the positive real property of $\lambda\tilde{\psi}(\lambda)$ it follows that the poles, $\{\pm i\omega_k\}$, and the zeros of $\lambda\tilde{\psi}(\lambda)$ alternate on the imaginary axis. Thus,

$$0 < \omega_1 < \tilde{\omega}_1 < \omega_2 < \cdots < \omega_k < \tilde{\omega}_k < \omega_{k+1}.$$

ε can now be considered. First, the open loop transfer function, equation (4), can be rewritten as

$$\psi_{Open} = \varepsilon + \tilde{\psi}(\lambda), \qquad \varepsilon > 0.$$

Hence, $\lambda(\varepsilon + \tilde{\psi}(\lambda))$ is positive real if $\lambda\tilde{\psi}(\lambda)$ is positive real (ε is positive). In particular, the zeros and poles of equation (4) also alternate on the imaginary axis; however, while the "pole" frequencies are not affected by ε, the "zero" frequencies are reduced. To see this, note that since

$$\psi_{Open}(i\tilde{\omega}_k) = \varepsilon + \tilde{\psi}(i\tilde{\omega}_k) > 0,$$

the following condition is necessary:

$$\psi_{Open}(i\tilde{\tilde{\omega}}_k) = \varepsilon + \tilde{\psi}(i\tilde{\tilde{\omega}}_k) = 0,$$

and subtracting $\psi_{Open}(i\tilde{\omega}_k)$ from $\psi_{Open}(i\tilde{\tilde{\omega}}_k)$ (using equation (10)) yields

$$0 < \omega_k < \omega_k < \tilde{\tilde{\omega}}_k, \qquad \text{for each } k.$$

Thus, electrical feedthrough reduces the frequencies at which the open loop transfer function is zero. Computational and experimental results in sections 6 and 7 validate this result.

5.3. CLOSED LOOP STABILITY

The focus of this section is on the stability of the closed loop system and its dependence on the compensator's tank frequency. The denominator of the closed loop transfer function, equation (7), can be rewritten as

$$g(\lambda; \alpha) = p(\lambda)D(\lambda) + \alpha\lambda(\varepsilon D(\lambda) + N(\lambda)), \tag{12}$$

where

$$N(\lambda) = \frac{1}{\gamma}\sinh(\gamma \cdot l)\cos(\gamma \cdot l) + \cosh(\gamma \cdot l)\sin(\gamma \cdot l), \tag{13}$$

$$D(\lambda) = [1 + \cosh(\gamma \cdot l)\cos(\gamma \cdot l)], \tag{14}$$

and where γ and $p(\lambda)$ were defined in section 5.1. To construct the root locus, let $\lambda(\alpha)$ denote a zero of $g(\lambda)$:

$$g(\lambda(\alpha); \alpha) = p(\lambda(\alpha))D(\lambda(\alpha)) + \alpha\lambda(\alpha)[\varepsilon D(\lambda(\alpha)) + N(\lambda(\alpha))] = 0. \tag{15}$$

Equation (15) defines $\lambda(\alpha)$ as a multivalued analytic function of α. Solving for α in equation (15) yields

$$\alpha = \left.\frac{-p(\lambda)D(\lambda)}{\lambda(\varepsilon D(\lambda) + N(\lambda))}\right|_{\lambda = \lambda(\alpha)}. \tag{16}$$

Equation (16) shows that α is zero whenever $p(\lambda)$ or $D(\lambda)$ are zero. This corresponds to the poles of the compensator or the poles of the open loop system. On the other hand, if α is infinity this corresponds to the denominator of equation (16) being zero, which occurs only at the frequencies of the zeros of the open loop transfer function or at $\lambda = 0$. Thus, equation (16) shows that the sequence of functions $\{\lambda_k(\alpha)\}$ will move from their open loop values $\{\lambda_k(\alpha = 0)\} = \{i\omega_k\}$, to $\{\lambda_k(\alpha = \infty)\} = \{i\tilde{\tilde{\omega}}_k\}$ (the zeros of the open loop system). On the other hand, equation (16) also shows how the functions $\lambda_c(\alpha)$, the circuit modes, move from their open loop values, $\lambda_c(\alpha = 0) \neq 0$, to their closed loop values $\lambda_c(\alpha = \infty) = 0$.

Having established the beginning, $\alpha = 0$, and the end, $\alpha = \infty$, of the root loci, the sign of the slope of departure for the analytic functions $\lambda_k(\alpha)$ can be derived. From equations (15) and (16) the derivative of $\lambda_k(\alpha)$ with respect to α is given by

$$\left.\frac{\mathrm{d}\lambda_k(\alpha)}{\mathrm{d}\alpha}\right|_{\substack{\alpha=0,\\ \varepsilon=0}} = \frac{(-i\omega_k)N(i\omega_k)}{p(i\omega_k)D'(i\omega_k)} = \frac{(-i\omega_k)}{p(i\omega_k)}\frac{b_k\omega_k^2}{2i\omega_k}$$

$$= \left[\frac{1}{2}b_k\omega_k^2 \cdot \frac{\left(\frac{\omega_k^2}{\omega_c^2} - 1\right)}{|p(i\omega_k)|^2}\right] + i\left[b_k\omega_k^3 \cdot \frac{RC}{|p(i\omega_k)|^2}\right] = \sigma_k'(0) + i\omega_k'(0). \qquad (17)$$

Note that $\omega_k'(0) > 0$ and

$$\sigma_k'(0) < 0 \text{ if } 0 < \omega_k < \omega_c, \qquad \text{and} \qquad \sigma_k'(0) > 0 \text{ if } 0 < \omega_c < \omega_k,$$

In particular, equation (17) shows that for small positive α:

$$\omega_k(\alpha) > \omega_k(0), \quad \sigma_k(\alpha) < 0 \text{ if } \omega_k < \omega_c, \qquad \text{and} \qquad \sigma_k(\alpha) > 0 \text{ if } \omega_k > \omega_c.$$

Hence, in the neighborhood of $\alpha = 0$ all system modes whose frequencies are lower than the tank frequency of the compensator will be stabilized, while all modes whose frequencies are higher than the tank frequency will be destabilized.

Next, it is necessary to show that these results also apply for every $0 < \alpha \leqslant \infty$.

Lemma 1 (Balakrishnan [1])

All closed loop modes with $\omega_k > \omega_c$ *are unstable for every* $0 < \alpha \leqslant \infty$.

Proof

This result has already been shown to hold in the neighborhood of $\alpha = 0$. Now, the emphasis is on showing that $\mathrm{Re}\,[\lambda_k(\alpha)] = \sigma_k(\alpha) > 0$ for $\omega_k > \omega_c$ and for all $0 < \alpha \leqslant \infty$. To show this by contradiction, assume that there exists an α_z such that

$$\sigma_k(\alpha_z) = 0; \qquad \sigma_k(\alpha) > 0, \qquad 0 < \alpha < \alpha_z,$$

but evaluating the imaginary part of equation (15) for the case where $\sigma_k(\alpha_z) = 0$ shows that $\omega = 1/\sqrt{LC} = \omega_c$, and using this to evaluate the real part of equation (15) yields the following necessary condition:

$$(\varepsilon + \psi(i\omega_c)) < 0.$$

The slope of $\sigma_k(\alpha_z)$ is obtained by taking the real part of the derivative with respect to α of $\lambda(\alpha)$, where $\lambda(\alpha)$ is obtained from equation (15),

$$\left.\frac{\mathrm{d}\sigma_k(\alpha)}{\mathrm{d}\alpha}\right|_{\substack{\alpha=\alpha_z,\\ \omega=\omega_c}} = \sigma_k'(\alpha_z) = \mathrm{Re}\left[\frac{(-i\omega_c)(\varepsilon+\psi(i\omega_c))}{\dfrac{2i}{\omega_c}+RC+\alpha_c\left(\varepsilon+\sum_1^{\infty}\dfrac{b_k\omega_k^2(\omega_k^2+\omega_c^2)}{(\omega_k^2-\omega_c^2)^2}\right)}\right]. \tag{18}$$

Inspection of equation (18) shows that $\sigma_k'(\alpha_z)$ has the same sign as $-(\varepsilon+\psi(i\omega_c))$ and since $(\varepsilon+\psi(i\omega_c))<0$ (a necessary condition) then $\sigma_k'(\alpha_z)>0$; but this is not possible at the point where $\sigma_k(\alpha\neq 0)=0$ for the first time. Hence,

$$\sigma_k(\alpha)>0 \ \text{ for every } \ \alpha>0.$$

Lemma 2 [1]

All closed loop modes with $\omega_k<\omega_c$ *are stable for every* $0<\alpha\leqslant\infty$.

Proof

This result has already been shown to hold in the neighborhood of $\alpha=0$. Now, following the arguments of Lemma 1, assume that there exists an α_z such that

$$\sigma_k(\alpha_z)=0; \qquad \sigma_k(\alpha)<0, \qquad 0<\alpha<\alpha_z$$

which implies that $\omega=1/\sqrt{LC}=\omega_c$ and the following necessary condition:

$$(\varepsilon+\psi(i\omega_c))<0.$$

But, since

$$\tilde{\omega}_k<\omega_c<\omega_{k+1},$$

it follows from the product expansion of $\psi(\lambda)$ that

$$\psi(i\omega)>0$$

which constitutes a contradiction because $\varepsilon>0$.

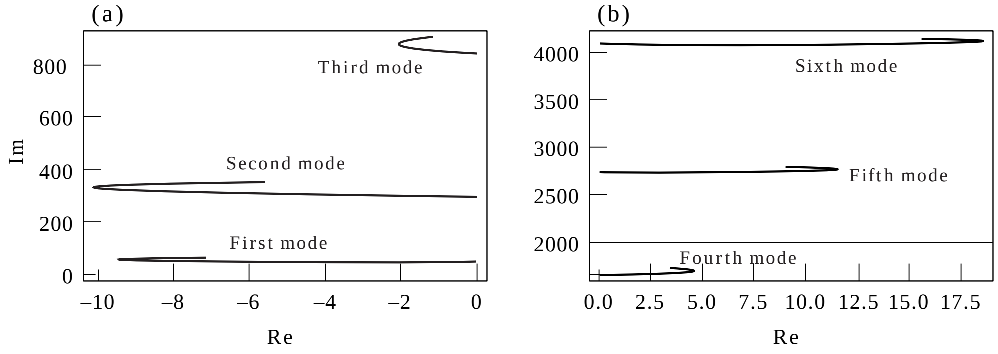

Figure 6. Simulated root loci: (a) modes 1–3, (b) simulated root loci modes 4–6.

5.4. ROOT LOCI SIMULATIONS

Equation (7) was used to generate Figures 6(a) and (b). These figures show the root loci (as a function of gain and for the first six modes only) for the beam and electronics described in sections 3 and 4 above (see Figures 3–5 and Table 1). For these simulations the tank frequency of the differentiator was set to 1118·41 rad/s (or 178 Hz). Note that starting with the fourth mode (1656·69 rad/s or 263·67 Hz) all closed loop beam modes are destabilized in contrast to the first three modes. Also, note that each root locus has a maximum (or minimum) real part.

6. BEAM TESTING AND VALIDATION

Once the beam was fabricated, tests had to be run to make sure the implants were not shorted, and that all wafers in each patch were indeed connected to each other. Also, the beam's dimensions, stiffness, and modal frequencies had to be measured and compared to the original design and computed values.

First, the capacitance of the implants was measured and the results are shown in Table 2. Note that the computed capacitance corresponds to unrestrained PZT, and the measured capacitance corresponds to restrained PZT (i.e., embedded in the fiber glass) which explains the large discrepancies. (The capacitance of restrained PZT is expected to drop by 10–20% in comparison to unrestrained PZT.)

By design the elastic modulus of the beam was tailored to construct a beam whose first modal frequency was near 7·8 Hz (this was the first modal frequency of the beam constructed by Lee [5]). The modulus computed for the desired geometry was $4{\cdot}2\,(10^{10})$ Pa ($6{\cdot}10\,(10^{6})$ psi). This number includes the effect of the PZT wafers embedded in the lay-up.

Experimentally, the modulus of the beam was estimated by applying a static force at the tip of the beam, measuring the resulting displacement, and then computing the modulus. Thus, the measured value of the equivalent Young's modulus was $4{\cdot}4\,(10^{10})$ Pa ($6{\cdot}375\,(10^{6})$ psi). The mass per unit length was also measured for the active portion of the beam, this measurement yielded 0·649 kg/m ($1{\cdot}13\,(10^{-3})$ slugs/in.).

The actuator moment output per DC voltage input was also measured. The maximum DC voltage available was ± 100 V. A DC voltage of 160 V

TABLE 2

Implant capacitance

Implant No.	Restrained PZT Measured (μF)	Unrestrained PZT Computed (μF)	% Difference
1	0·640	0·764	16·2
2	0·604	0·764	20·9
3	0·626	0·764	18·0
4	0·650	0·764	14·9

(± 80 v) was applied to the actuator. The tip displacement produced by this voltage was 0·0012 m (3/64 in.). The tip moment corresponding to this displacement is 0·085 N-m (0·7529 lbf-in.). This measurement implies an actuator constant (static) of 532·0 (10^{-6}) N-m/V (0·471 (10^{-2}) lbf-in./V). Similarly, the PZT sensor constant was measured as 655·6 V/rad, where the angle measured is the angle of the beam at its free tip.

6.1. OPEN LOOP POLES AND ZEROS

The open loop poles and zeros of the beam were measured through the PZT sensor/actuator pair embedded in the beam. To do this, the actuator was driven by white noise, and the sensor response was recorded. A Bode plot of the measured transfer function of the beam was then computed, and the frequencies of the poles and zeros of the beam were read from the plot.

Figure 7(a) shows the experimental set-up used to obtain the open loop poles and zeros of the beam. Figure 7(b) shows the simulated bode plot of the transfer function of the beam using equation (4). Table 3 shows the computed and measured open loop pole and zero frequencies as well as their corresponding percentage damping.

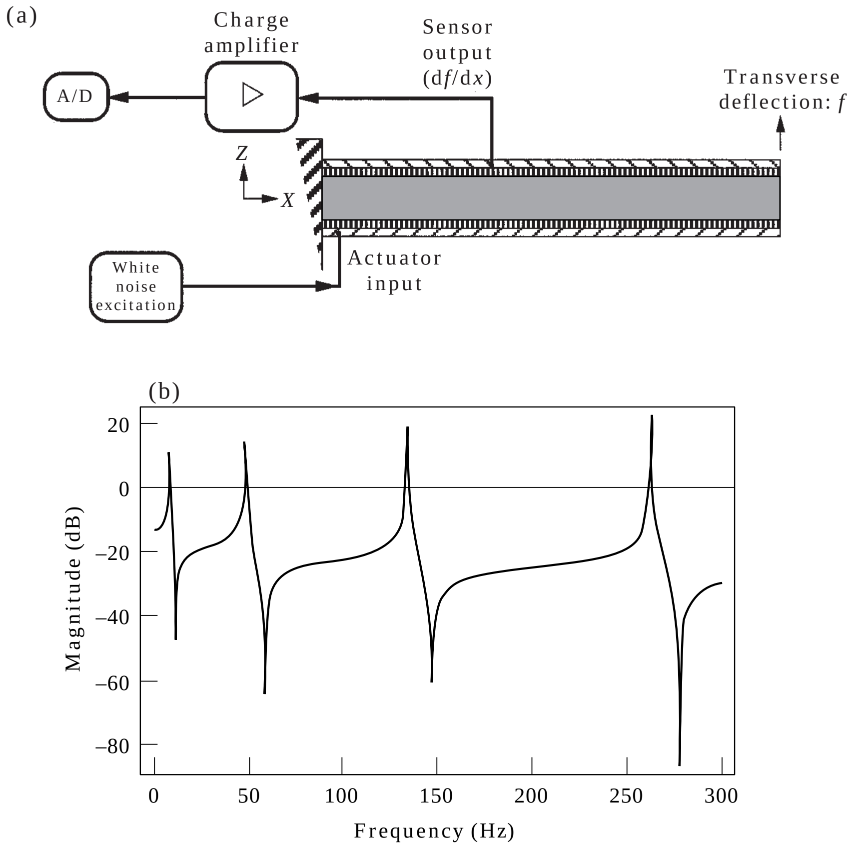

Figure 7. (a) Open loop experimental set-up; ⧅, sensor; ▨, actuator; ■, beam's core; □, implants not used. (b) Simulated open loop transfer function Bode plot.

TABLE 3

Pole and zero frequencies and % damping

	Poles				Zeros		
No.	Computed frequencies (Hz) [$\varepsilon = 0$]	Computed frequencies (Hz) [$\varepsilon = 0{\cdot}0022$]	Experiment (Hz)	Experiment Damping (%)	Computed frequencies (Hz) [$\varepsilon = 0$]	Computed frequencies (Hz) [$\varepsilon = 0{\cdot}0022$]	Experiment frequencies (Hz) No compensation
1	7·67	7·67	7·81	0·50	12·16	10·96	11·00
2	48·05	48·05	49·60	0·45	65·70	58·40	59·20
3	134·50	134·50	138·00	0·40	162·27	147·60	142·00
4	263·67	263·67	272·00	0·40	301·74	278·60	284·00

Note the two sets of computed frequencies for both the poles and zeros of the beam shown in Table 3. The first of the two columns in each case corresponds to frequencies computed using equation (4) with the electrical feedthrough term set to zero. The second of the two columns corresponds to frequencies computed using equation (4) but with the feedthrough term set to an experimentally determined positive value (more about this in the next section). As discussed in section 5, pole frequencies were not affected by the electrical feedthrough. On the other hand, computed zero frequencies were reduced by electrical feedthrough, as predicted in section 5. The reduction of the zero frequencies is verified by experimental results also shown in the table.

Table 3 also shows the measured structural damping for each of the first four modes. This inherent structural damping, not modelled in section 5, precludes the destabilization of higher frequency modes by the feedback compensator (as predicted in section 5).

6.2. ELECTRICAL FEEDTHROUGH

The lack of shielding between sensor and actuator caused electrical feedthrough between them. This effect reduces the frequency of the transmission zeros, but does not affect pole frequencies. Since the transmission zeros influence the performance of the rate feedback compensator [1, 5], it is necessary to model and estimate the actual levels of feedthrough. Thus, the feedthrough was modelled as being directly proportional to the actuator's input voltage, see equation (2).

The proportionality constant, ε, is found experimentally by iteratively subtracting from the measured sensor voltage, V_m, a voltage proportional to the actuator's input voltage (in open loop). The resulting "compensated" voltage is then used to compute the open loop transmission zeros. ε is fixed when the zeros thus computed match the predicted zeros of a "tuned" model (tuned to the experimentally determined poles of the beam) in which the feedthrough effect is neglected. Thus, ε was found to be 0·0022. This value of ε was used in equation (4) to compute the transmission zero frequencies of the system, which can be compared to the zero frequencies determined experimentally (see Table 3).

Although this technique for determining the value of ε could be substituted with a computational iterative procedure using equation (4), the experimental

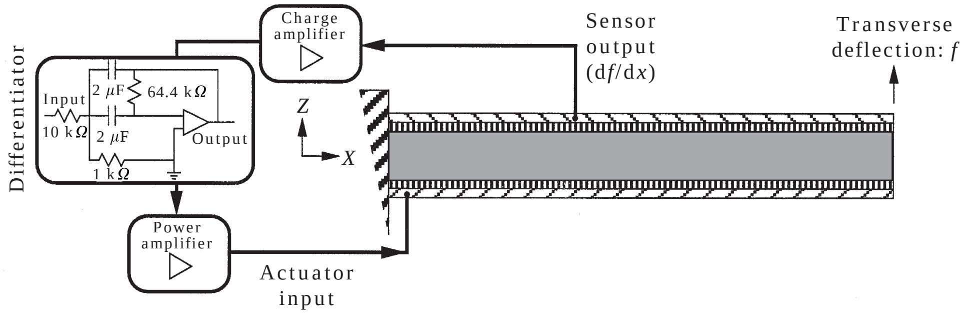

Figure 8. Closed loop experimental set-up: experiment 1.

procedure used here offers two advantages. First, if the "zero" frequencies of the open loop compensated system (as described in the last paragraph) can be increased enough to match the "zero" frequencies of a system without feedthrough, then this justifies the model for ε used in section 5. Second, the possibility of changing "zero" frequencies for the system (through the use of a secondary feedback loop) offers an increase of performance and robustness to control schemes that rely on the location of such zeros (i.e., pole/zero placement, pole/zero cancellation, etc.). Further research on this seems plausible.

7. CLOSED LOOP EXPERIMENTS

Two closed loop experiments are described here. For the first experiment, the tank frequency of the differentiator was placed between the first and the second modes. For the second experiment the tank frequency of the differentiator was set between the third and fourth modes. The primary goal of these experiments is to show the stabilization of modes prior to the tank frequency, and the destabilization of modes after the tank frequency.

7.1. EXPERIMENT 1

In this experiment the differentiator's tank frequency was set between the first and second modes of the clamped–free beam (tank frequency at about 10·44 Hz), and the gain was set to 2·7. The intention here was to demonstrate how the

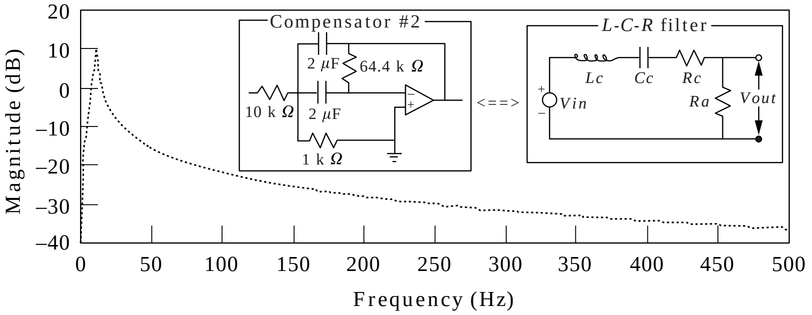

Figure 9. Transfer function Bode plot of differentiator: experiment 1.

damping in the first mode can be improved while setting the second mode unstable. Figure 8 depicts the closed loop experimental set-up for this experiment. The transfer function of the differentiator used, its circuit diagram and equivalent circuit are depicted in Figure 9.

The experiment was conducted as follows. First, the free tip of the cantilevered beam was deflected 2·54 (10^{-3}) m (0·1 in.) and then released. Thus, the beam's first mode was excited, and the beam was allowed to vibrate for about 3 s. Then, the loop of the compensator was closed. After closing the loop, the beam stopped vibrating at its first modal frequency and began vibrating at its second modal frequency. Then, the magnitude of vibration of the second mode increased in magnitude until all circuits saturated. At this point the loop was opened.

This response of the beam during this process was recorded using the PZT sensor on the beam, a personal computer, the National Instruments E1 data acquisition board and a *Virtual Instrument* created in LabVIEW®. Figure 10 shows the beam's response as a function of time.

Figure 10 clearly shows how the first mode of the beam is damped after closing the loop. The amount of damping added to this mode was estimated by filtering all higher frequencies in the data and measuring the logarithmic decrement of the response after the loop was closed. The damping thus estimated was 7·4% (up from 0·5%). Figure 10 also shows how the beam starts vibrating at its second modal frequency, and it continues to do so without bound (other than the eventual circuit saturation). Thus, the rate feedback used here is clearly stabilizing the first mode and destabilizing the second as predicted in section 5.

Although the second mode is being destabilized, there is no evidence in Figure 10 that higher modes are also being destabilized as predicted earlier. To understand this discrepancy, first note that the beam model give in section 5 did not include the structural damping inherent in the beam; thus, destabilization of modes whose frequencies are higher than the differentiator's tank frequency is prevented by the inherent damping unless the gain of the feedback loop is

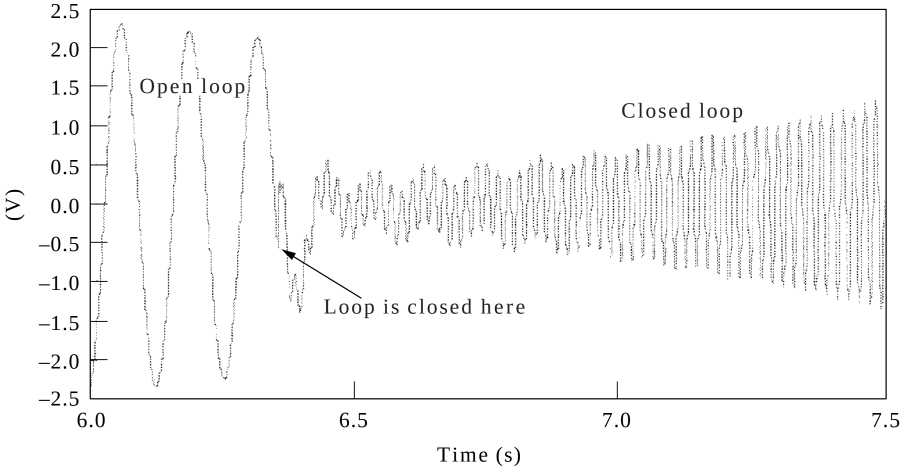

Figure 10. Closed loop response of beam measured by PZT sensor: experiment 1.

sufficiently high. This is in effect the phenomenon observed here. For example, when the gain was reduced by 10%, the second mode was no longer destabilized. This observation also suggests that it is possible to design and implement a stable system (i.e., with negative real part for all closed loop poles), of the type constructed here, as long as certain guidelines are observed.

7.2. EXPERIMENT 2

In this experiment the differentiator's tank frequency was set between the third and fourth modes (tank frequency at 178 Hz). The goal of this experiment was to demonstrate how a stable system can be achieved. According to reference [1], the damping in the first three modes should increase as the loop gain increases, while the fourth mode (and higher ones) should be destabilized.

The experimental set-up used here was as depicted in Figure 8. The differentiator's circuitry and transfer function are shown in Figure 3. Figures 11(a) and 11(b) show the computed damping values as functions of loop gain (first six modes only). For these calculations equation (7) and the system parameters given in Table 1 were used to compute the root loci for the first six modes. Damping values were then extracted from each of the root loci. Note how the negative damping in the first three modes first increases (reaching a maximum value) and then decreases with increasing loop gain. On the other hand, the positive damping in the fourth and higher modes follows the same pattern.

Figure 12 shows the experimental open and closed loop transfer function Bode plots of the beam from PZT sensor to PZT actuator (the closed loop gain was set to 60). Again, the damping for the first three modes was increased, while the damping in the fourth mode was decreased (this is evident from the narrowing of the fourth mode's peak). In particular, measurement of the first mode's damping yielded −12·0%; its open loop value was −0·50%. And, measurement of the fourth mode's damping yielded −0·1%; its open loop value was −0·4%.

When the gain was increased to 70, the sixth mode of the beam 651 Hz became unstable (instead of the fourth or fifth modes). This can be anticipated from Figures 11(a) and (b) which shows that more damping is subtracted from the sixth mode than any other mode, and from knowledge of the open loop damping levels (about 0·4% for the first few modes).

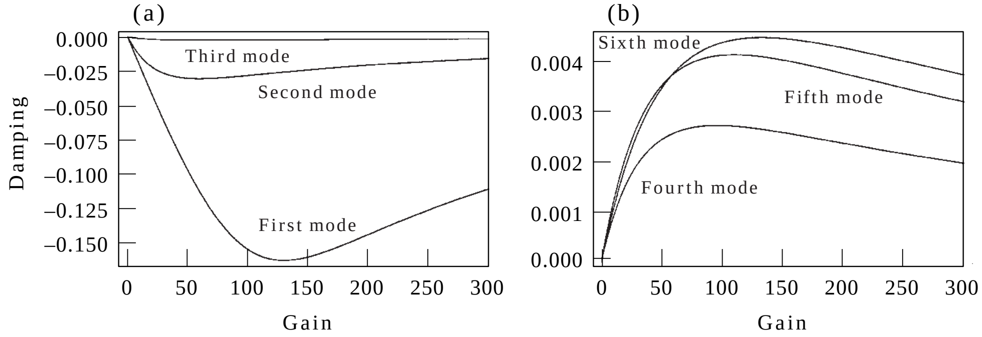

Figure 11. Computed damping performance: (a) modes 1–3, (b) modes 4–6.

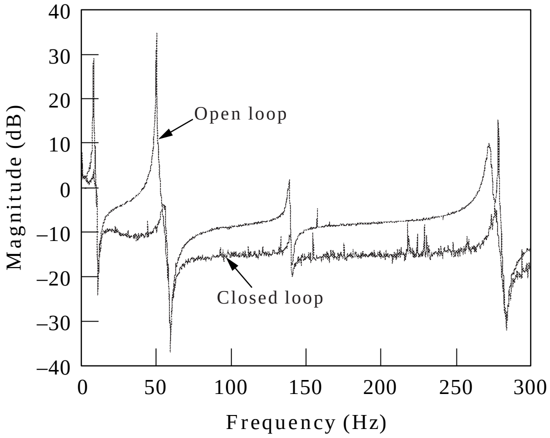

Figure 12. Open versus closed loop transfer functions: experiment 2; tank frequency of differentiator at 178 Hz; gain set at first mode's critical value ($Rf = 11{\cdot}7$ K).

The open loop transfer function Bode plot shown in Figure 12 should be compared to the computed one in Figure 7(b). The measured frequency response shown in Figure 12 is higher than the computed one in Figure 7(b) by a constant. This discrepancy was caused by measurement of the excitation signal before its amplification stage shown in Figure 3. The resonant frequencies of the two figures were already compared in Table 3 where the percentage error in the computed values was less than 5%. Damping was experimentally measured to be less than 0·5% for the first four modes, whereas the mathematical model of section 5 did not include any damping. The absence of damping in the model was emphasized by the relatively low amplitude response of the beam at its third mode, shown in Figure 12, in comparison to what was computed and shown in Figure 7(b).

8. CONCLUSIONS

Experiments with a strain actuated beam have helped verify Balakrishnan's findings [1]. Laboratory experiments, in agreement with computational predictions, have demonstrated how rate feedback compensation for a clamped–free beam stabilizes some modes while destabilizing others (in contrast to stabilizing all modes [8]). This phenomenon is due to the non-ideal implementation of the differentiator, thus showing the importance of modelling the controller's circuitry.

Modelling the controller's circuitry in the conext of self-strained structural systems was introduced by Balakrishnan [1]. In the work presented here, continuum models of strain actuated systems and their associated controller electronics are referred to as *circuitry enhanced models*. This work also appears to be the first time a *circuitry enhanced model* for a self-strained beam and associated controller is corroborated by laboratory experiments.

The presence of inherent structural damping in the beam, not modelled here, maintains closed loop stability as long as the feedback loop gain remains sufficiently small. This means that the stability of strain actuated beams (like the one studied here) can only be *partially* enhanced: "While the stability margin of all modes below the differentiator's tank frequency is increased, the stability of all remaining modes is decreased (when compared to their open loop stability margin); and, for a sufficiently small feedback gain, the overall system remains stable".

ACKNOWLEDGMENTS

This work was partially supported by the Spacecraft & Technology Division of TRW Inc., and by NASA grant NCC 2-374. The authors greatly appreciate the guidance and support of Professor A.V. Balakrishnan. Special thanks to Ted Nye, George Dvorsky and Art Rico of TRW who made the fabrication of our strain actuated beam possible, and to Christopher Kuehl for helping with the measurements.

REFERENCES

1. A. V. Balakrishnan 1999 *Journal of Computational and Applied Mathematics* **18**. Damping performance of strain actuated beams.
2. T. Bailey and J. E. Hubbard, Jr. 1985 *Journal of Guidance and Control* **8**, 605–611. Distributed piezoelectric-polymer active vibration control of a cantilever beam.
3. H. S. Tzou and M. Gadre 1989 *Journal of Sound and Vibration* **132**, 433–450. Theoretical analysis of a multi-layered thin shell coupled with piezoelectric shell actuators for distributed vibration controls.
4. H. S. Tzou, D. D. Johnson and K. J. Liu 1995 *Wave Motion*, *Intelligent Structures and Nonlinear Mechanics* **1**, 163–193. Nonlinear control and boundary transition of cantilevered distributed systems.
5. C.-K. Lee, W.-W. Chiang and T. C. O'Sullivan 1991 *Journal of the Acoustic Society of America* **90**, 374–384. Piezoelectric modal sensor/actuator pairs for critical active damping vibration control.
6. G. Chen *et al*. 1987 *Operator Methods for Optimal Control Problems* **108**, 67–96. The Euler–Bernoulli beam equation with boundary energy dissipation.
7. A. Baz and S. Poh 1988 *Journal of Sound and Vibration* **126**, 327–343. Performance of an active control system with piezoelectric actuators.
8. A. V. Balakrishnan 1997 in *Smart Structures and Materials* 1997: *Mathematics and Control in Smart Structures* (V. V. Varadan and J. Chandra, editors) **3039**, 204–215. Theoretical limits of damping attainable by smart beams with rate feedback.